

# Automatic segmentation of Organs at Risk in Head and Neck cancer patients from CT and MRI scans.

Sébastien Quetin<sup>1,2</sup>, Andrew Heschl<sup>3</sup>, Mauricio Murillo<sup>3</sup>, Murali Rohit<sup>4</sup>, Shirin A. Enger<sup>1,2,5,\*</sup>, and Farhad Maleki<sup>3,6,7,\*</sup>

<sup>1</sup>Medical Physics Unit, Department of Oncology, McGill University, Montreal, QC, Canada

<sup>2</sup>Montreal Institute for Learning Algorithms, Mila, Montreal, QC, Canada

<sup>3</sup>Department of Computer Science, University of Calgary, Calgary, AB, Canada

<sup>4</sup>Cloud Innovation Center, University of British Columbia, BC, Canada

<sup>5</sup>Lady Davis Institute for Medical Research, Jewish General Hospital, Montreal, QC, Canada

<sup>6</sup>Department of Diagnostic Radiology, McGill University, Montreal, QC, Canada

<sup>7</sup>Department of Radiology, University of Florida, Gainesville, FL, USA

\*Co-supervisor for this research.

April 2024

**Short title:** Multimodal auto-segmentation in Head and Neck organs.

**Corresponding author:** Sébastien Quetin, [sebastien.quetin@mail.mcgill.ca](mailto:sebastien.quetin@mail.mcgill.ca)

**Keywords:** Head and Neck cancer, Organs at risk, Segmentation, Deep Learning, Multi-modality

**Sources of support:** Canada Research Chair Program, Google's exploreCSR program, the University of British Columbia Cloud Innovation Centre, Calcul Quebec and the Digital Research Alliance of Canada, and the University of Calgary Advanced Research Computing Cluster.

# 1 Abstract

**Background and purpose:** Deep Learning (DL) has been widely explored for Organs at Risk (OARs) segmentation; however, most studies have focused on a single modality, either CT or MRI, not both simultaneously. This study presents a high-performing DL pipeline for segmentation of 30 OARs from MRI and CT scans of Head and Neck (H&N) cancer patients.

**Materials and methods:** Paired CT and MRI-T1 images from 42 H&N cancer patients alongside annotation for 30 OARs from the H&N OAR CT & MR segmentation challenge dataset were used to develop a segmentation pipeline. After cropping irrelevant regions, rigid followed by non-rigid registration of CT and MRI volumes was performed. Two versions of the CT volume, representing soft tissues and bone anatomy, were stacked with the MRI volume and used as input to an nnU-Net pipeline. Modality Dropout was used during the training to force the model to learn from the different modalities. Segmentation masks were predicted with the trained model for an independent set of 14 new patients. The mean Dice Score (DS) and Hausdorff Distance (HD) were calculated for each OAR across these patients to evaluate the pipeline.

**Results:** This resulted in an overall mean DS and HD of  $0.777 \pm 0.118$  and  $3.455 \pm 1.679$ , respectively, establishing the state-of-the-art (SOTA) for this challenge at the time of submission.

**Conclusion:** The proposed pipeline achieved the best DS and HD among all participants of the H&N OAR CT and MR segmentation challenge and sets a new SOTA for automated segmentation of H&N OARs.

## 2 Introduction

Head and Neck (H&N) cancer ranks as the seventh most prevalent cancer globally, encompassing a heterogeneous array of cancers impacting the upper aerodigestive tract [1]. Radiotherapy, one of the most common treatments for H&N cancers [2], aims to deliver a high radiation dose to tumorous tissues while sparing the surrounding healthy tissues. Segmentation of Organs At Risk (OAR) is an important step in radiotherapy treatment planning, essential for optimizing treatment plans and assessing their quality [3]. Manual segmentation of OAR is labor-intensive and prone to inter-observer variability [4]. While Deep Learning (DL) techniques have been applied for automated OAR segmentation, most studies focus on either CT or MRI scans separately, neglecting to utilize both modalities simultaneously [5]. This might happen because not every patient undergoes both CT and MRI scans. Due to MRI scans offering superior soft tissue contrast [6, 7], several studies have concentrated on synthesizing MRI images from CT scans, aiming to facilitate organ segmentation from these synthesized MRI volumes [8, 9, 10, 11, 12, 13, 14, 15]. Some studies have devised methods capable of segmenting organs interchangeably from both modalities in cardiac [16] and abdominal images [17]. Some studies used both modalities for segmenting organs in prostate [18] and H&N [19] cancer patients. The former directly learns from a weighted sum of the two modalities. The latter devised a method that learns from both modalities separately and combines the features learned to predict OAR contours.

In this study, a DL-based pipeline utilizing both MRI and CT scans was developed to automatically segment 30 OARs in H&N cancer patients from both MRI and CT scans, whether used individually or jointly.

### 3 Materials and Methods

This section provides detailed information about the proposed approach for OAR segmentation in H&N cancers, utilizing both CT and MRI scans. The proposed approach enhances the nnU-Net pipeline, which is the state-of-the-art (SOTA) across many unimodal segmentation tasks [20], and expands its utility to multimodal segmentation tasks. The proposed approach utilizes customized preprocessing, model training, and postprocessing steps to allow for the effective utilization of both CT and MRI scans for segmentation tasks. Figure 1 presents a schematic overview of the proposed approach, and the following subsections delve into each aspect of the customized nnU-Net model for multimodal processing of CT and MRI scans.

#### 3.1 Dataset

The H&N OARs CT and MR segmentation dataset [5] was released as part of an international challenge for H&N OAR segmentation. The dataset comprises CT and MRI-T1 scans of 42 H&N patients and contours for 30 OARs provided for the CT scans. This dataset was used to train the developed segmentation pipeline. A different, independent test set of 14 new patients, accessible indirectly through the challenge platform, was used to evaluate the pipeline performance.

The field of view of the MRI volume was consistently smaller than the field of view of the CT volume. As a result, for some patients certain OARs were not present in the MRI volume. The OARs concerned are the arytenoid cartilage, the cricopharyngeal inlet, the cervical esophagus, the thyroid gland and the larynx supraglottic.

#### 3.2 Cropping

In the provided dataset, a significant portion of the CT and MRI images consist of background, mainly attributed to air or the patient’s table. These background regions are not useful to the segmentation of H&N OARs. To reduce the volume sizes and facilitate model training while preserving the OARs, the CT volumes were cropped using the following mechanism. Outside body volume (air) was first cropped using a thresholding approach. Then, the minimum and maximum distances from the CT origin to a voxel belonging to any OAR were computed across all patient scans in the dataset on each axis. Volumes were cropped utilizing these limits extended with a margin of 20 mm on each side of each axis. When a cropping boundary exceeded the patient’s volume, the new cropping boundary became the patient’s volume boundary. The MRI volumes were not cropped at this stage, as they were implicitly cropped by the registration process (see below).

#### 3.3 Registration

A rigid (affine) followed by a non-rigid (B-spline) registration was performed using the SimpleITK toolkit [21] to align CT and MRI scans. Each CT scan was set as the fixed volume, and its corresponding MRI was set as the moving volume. The negative Mutual Information (MI) [22, 23] was minimized for both rigid and non-rigid registration. More details regarding the implementation of our registration pipeline can be found in Appendix A.

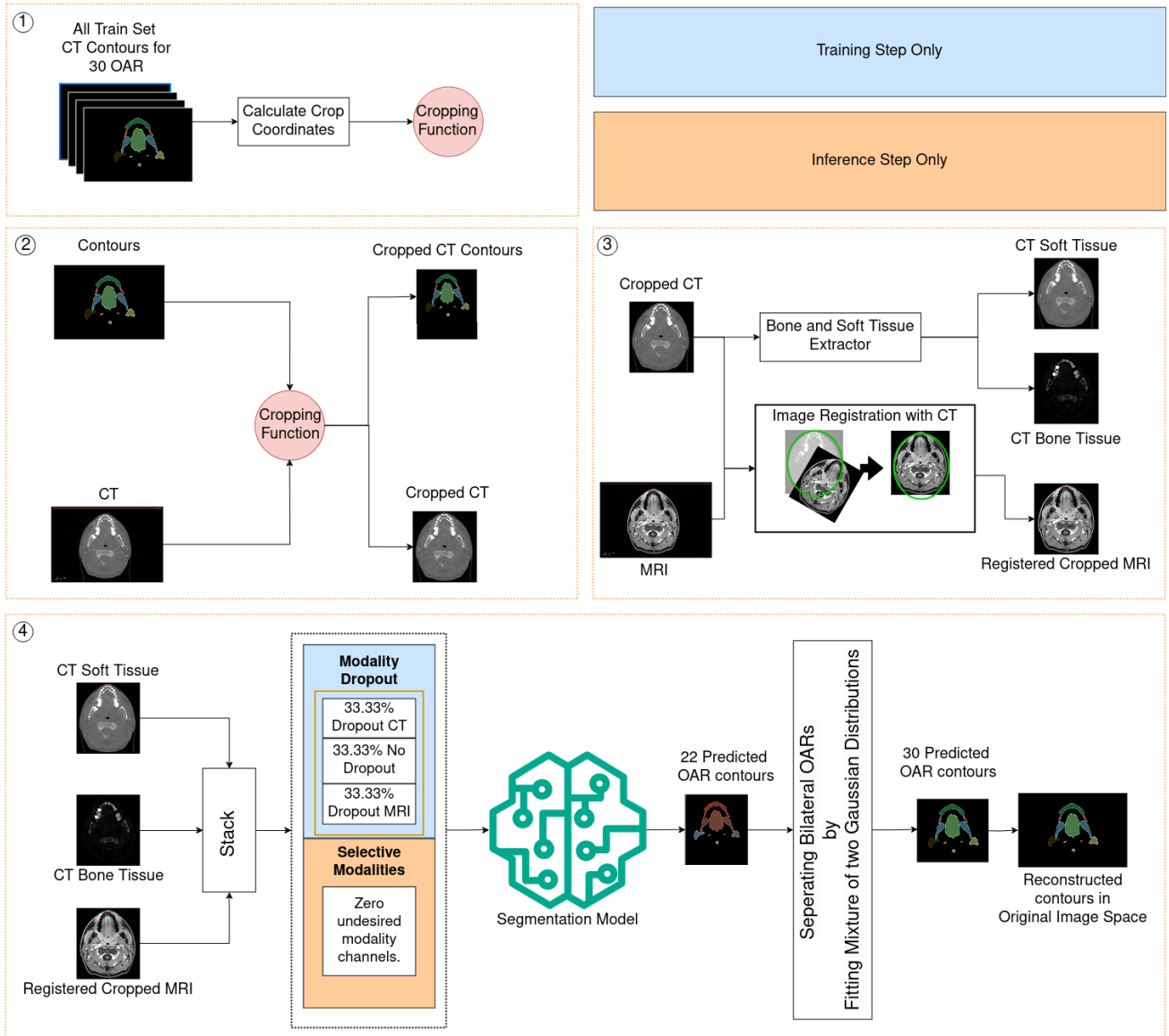


Figure 1: A schematic overview of the proposed approach: Both training and inference follow the proposed registration and OAR separation. When training, modality dropout is employed. When running inference, only one modality is necessary for the pipeline to predict contours. In the case where only one modality is used, the remaining modality is set to zeroes.

### 3.4 Preprocessing

OAR categories representing bilateral OARs (e.g., right and left optic nerves) were combined as one component during training, resulting in 22 OAR categories—a reduction from 30 OARs.

Two separate volumes were produced from the CT scan data: one focusing on soft tissue and the other on bone. The soft tissue volume was standardized to the Hounsfield Unit (HU) range of -500 to 500, using the mean and standard deviation of the voxel values within this range in the dataset. Likewise, bony tissue volume was generated using a similar process using the HU range of 0 to 3000. The MRI volume was also standardized, where both the mean and standard deviation were calculated using only the voxels registered to CT voxels within the aforementioned range for soft tissue.

### 3.5 Training

The MRI and the two generated CT volumes were stacked in a vector as input to the nnU-Net pipeline. Default parameters were used for model architecture with the 3D full-resolution model. A 5-fold cross-validation was used to train five models, each for 1000 epochs, on different splits (training 80%/validation 20%) of the dataset. The Dice-Cross Entropy sum, which is the summation of the Dice loss and Cross Entropy loss, was used as the loss function. All default nnU-Net augmentations, including spatial transformations, were used. To help generalize despite the small dataset size, the elastic deformation augmentation was enabled. Mirroring augmentation was only activated across the sagittal axis.

To accommodate learning from both data modalities, i.e. CT and MRI scans, the nnU-Net model architecture was customized by incorporating a Modality Dropout [24, 25, 26]. The developed Modality Dropout randomly selected one of the following three scenarios with equal probability: (1) only the two CT channels were utilized while the MRI channel was set to zero, (2) only the MRI channel was utilized while the CT channels were zeroed out, or (3) all three channels were used simultaneously. The best model in each fold was chosen to be the model with the lowest validation loss value during training and was then used for inference.

### 3.6 Inference and post processing

A test-time augmentation was used by flipping volumes across the sagittal axis, resulting in two different volumes. The model raw outputs, referred to as logits, for these volumes were then averaged after flipping back the output if the respective input was originally flipped. This operation was performed for the five best models, one from each fold. Mean logits obtained from each of the five models were averaged, and the results were converted to segmentation masks using the argmax operation.

Since bilateral OARs—i.e., OARs with left and right components—were combined into a single component for training and inference, the pipeline’s predicted segmentation masks were split to create the left and right components for those OARs. This was achieved by fitting a mixture of two Gaussian distributions to the voxel positions of the predicted contour. As left and right organs never overlapped in the training dataset, the mean of the Gaussian mixture was used as a threshold to separate such OARs into left and right OARs.

## 3.7 Evaluation

### 3.7.1 Testing

An external evaluation was performed on the test set through the [Head and Neck Organ-At-Risk CT & MR Segmentation Challenge](#) website. This external test set was not directly accessible to the participants. As such, the developed pipeline was submitted to the challenge platform to make predictions.

### 3.7.2 Ablation study

Internal evaluation was performed locally to validate our pipeline design choices as part of our ablation study. The first fold model was randomly chosen for this validation. The other four fold models were not used. Predictions were made on the corresponding internal validation set for the different experiments of the ablation study. It consisted of 20% of the dataset, while the remaining 80% was used for model training.

Two different experiments were conducted to evaluate the effect of the Modality Dropout and dataset composition. First, the model was trained on the dataset presented in Section 3.4, but without the Modality Dropout augmentation.

Then, to evaluate the impact of having left and right contours from the same organs, the model was trained following the training procedure presented in Section 3.5 (including Modality Dropout), with the 30 original OAR ground truth without combining left and right organs. For this particular training, and to avoid sending a counterproductive signal to the model considering the left and right position of the OAR, neither mirroring nor test-time augmentation was used for inference.

These model performances were compared in terms of Sørensen-Dice coefficient (Dice Score) and Hausdorff Distance at the 95<sup>th</sup> Percentile (Hausdorff Distance) to the performance of the model from the first fold on the internal validation dataset of the first fold. The results were first averaged for each OAR across all cases; then averaged once more across all OARs.

## 4 Results

### 4.1 Registration

Rigid registration took on average 20 seconds  $\pm$  7 seconds, and total registration time, including rigid and non-rigid registration, took on average 126 seconds  $\pm$  64 seconds. Appendix B showcases an example of registered MRI scan.

### 4.2 Challenge performance on an external dataset

The strict time requirement of the challenge submissions enforced that the segmentation of the 30 OARs for one patient would not exceed 15 minutes on a machine with 32GB RAM and a Graphics Processing Unit with 16 GB of VRAM. The proposed approach obtained a performance of  $0.777 \pm 0.118$  and  $3.455 \pm 1.679$  as the mean Dice Score and Hausdorff Distance, respectively.

Appendix C presents the mean Dice score and the mean Hausdorff Distance obtained by the proposed approach on the test set for each OAR. The mean Dice score ranges from 0.411 for the

Optic Chiasm to 0.952 for the Mandible bone. The mean Hausdorff Distances range from 1.289 for the Mandible bone to 7.661 for the Cervical esophagus.

Algorithm	Mean Dice Score $\uparrow$	Mean Hausdorff Distance $\downarrow$
the_HaN-Seg23_game	0.768 $\pm$ 0.119	3.542 $\pm$ 1.623
han_seg	0.768 $\pm$ 0.118	3.793 $\pm$ 1.797
HaNSeg_zhack	0.750 $\pm$ 0.125	3.714 $\pm$ 1.610
hanseg3	0.751 $\pm$ 0.117	3.869 $\pm$ 1.831
HandNSeg (Ours)	<b>0.777</b> $\pm$ 0.118	<b>3.455</b> $\pm$ 1.679

Table 1: Comparison with top-ranked challenge submissions: The reported measures are in the form of mean  $\pm$  standard deviation. The performance measures for each OAR were first averaged across all cases, and then the resulting values were averaged across all organs to calculate the overall model performance.  $\uparrow$  indicates that higher values are better and  $\downarrow$  indicates lower values are better.

Table 1 presents the results of the best submission of the top 5 teams in the challenge. The proposed approach resulted in the best Dice Score and the best Hausdorff Distance.

### 4.3 Ablation study

Table 2 shows the segmentation performance of the developed pipeline with and without the Modality Dropout for three scenarios: only using CT, only using MRI, and jointly using both CT and MRI. As explained in Section 3.1, when prediction are exclusively based on MRI data, some OARs are not present in the input volume and thus not included in the calculation of mean segmentation metrics, which are averaged over 25 OARs instead of 30.

The results show that a model trained with Modality Dropout can predict from both modalities used jointly or separately. The model trained without Modality Dropout resulted in a negligible Dice Score when CT information was missing, indicating that the trained model heavily relies on CT images and cannot perform well when missing CT scans; however, using Modality Dropout during the training makes the model much more robust to missing modalities. A similar behavior was observed when evaluating the model using the Hausdorff Distance. Finally, when predicting with both modalities as inputs, both models obtained similar Dice Scores, but the model trained with Modality Dropout obtained a better Hausdorff Distance.

Performance	With Modality Dropout			Without Modality Dropout		
	CT only	MRI only	CT + MRI	CT only	MRI only	CT + MRI
<b>Dice Score <math>\uparrow</math></b>	0.758 $\pm$ 0.125	0.57 $\pm$ 0.181	0.759 $\pm$ 0.125	0.751 $\pm$ 0.121	0.037 $\pm$ 0.106	<b>0.76 <math>\pm</math> 0.125</b>
<b>Hausdorff Distance 95 <math>\downarrow</math></b>	3.25 $\pm$ 1.655	7.124 $\pm$ 7.791	<b>3.236 <math>\pm</math> 1.666</b>	3.42 $\pm$ 1.701	NaN	3.937 $\pm$ 3.702

Table 2: Segmentation metrics obtained by comparing predictions of our pipeline trained with and without Modality Dropout to the challenge ground truth contours of our internal validation set. Results were first averaged over all cases and finally over all organs.  $\uparrow$  indicates that higher is best and  $\downarrow$  indicates smaller is best. As described in Section 3.1, the segmentation metrics obtained with MRI only are not averaged over 30 OARs but 25.

Figure 2 presents the pipeline prediction for a patient in the internal validation set. As shown, if the model only predicts from the MRI modality, it can only predict organs in the field of view of the MRI scan. Figure 3 shows the prediction of the larynx contour using the model trained

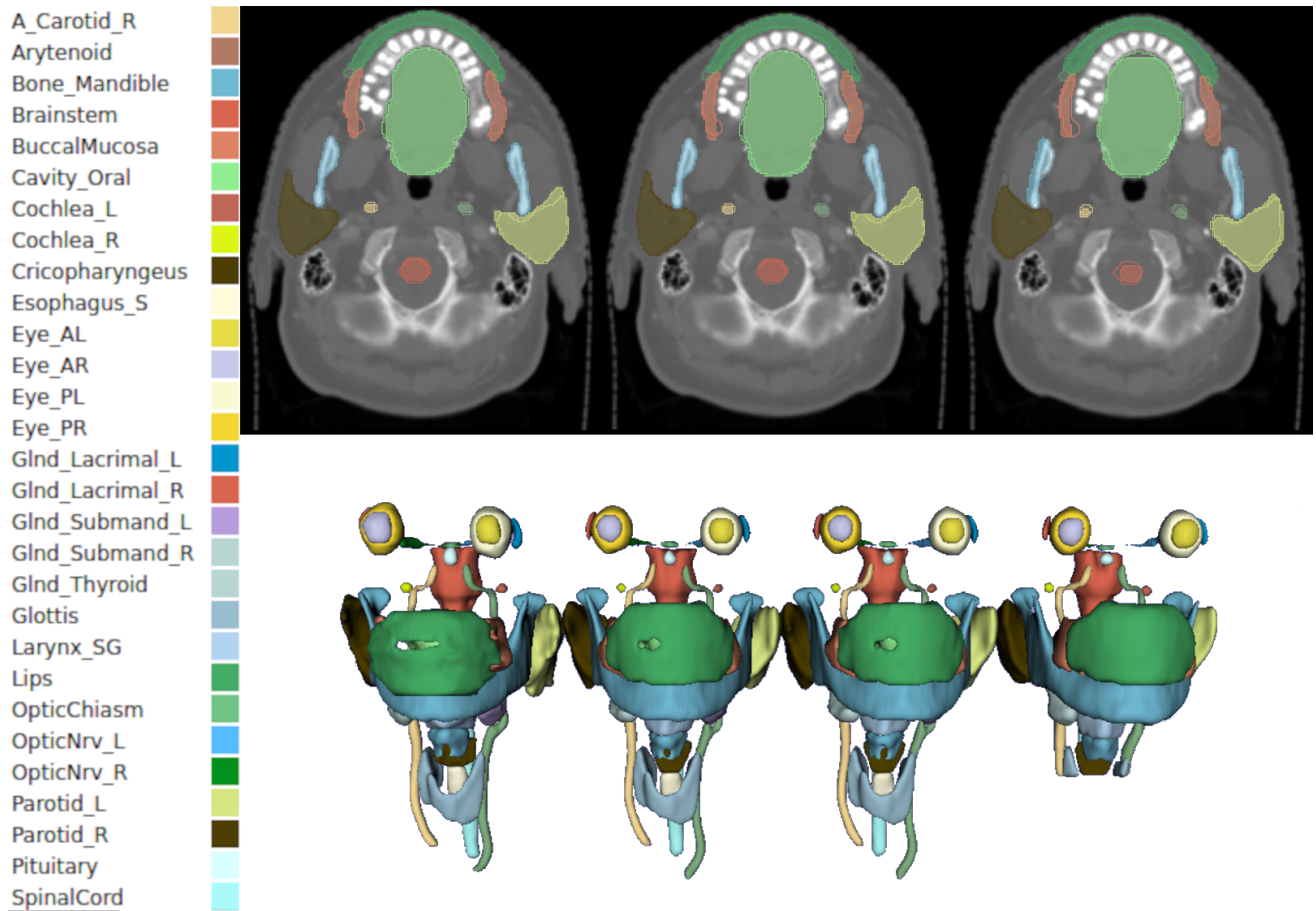


Figure 2: Prediction of a model trained with Modality Dropout, on case 22 of the Head and Neck Organ-at-Risk CT & MR Segmentation Challenge. From left to right, the top row shows the prediction with both modalities: CT and MRI. Ground truth is represented as an outline, and the prediction is filled in. The second row shows from left to right the ground truth, the prediction with both modalities, only CT, and only MRI.



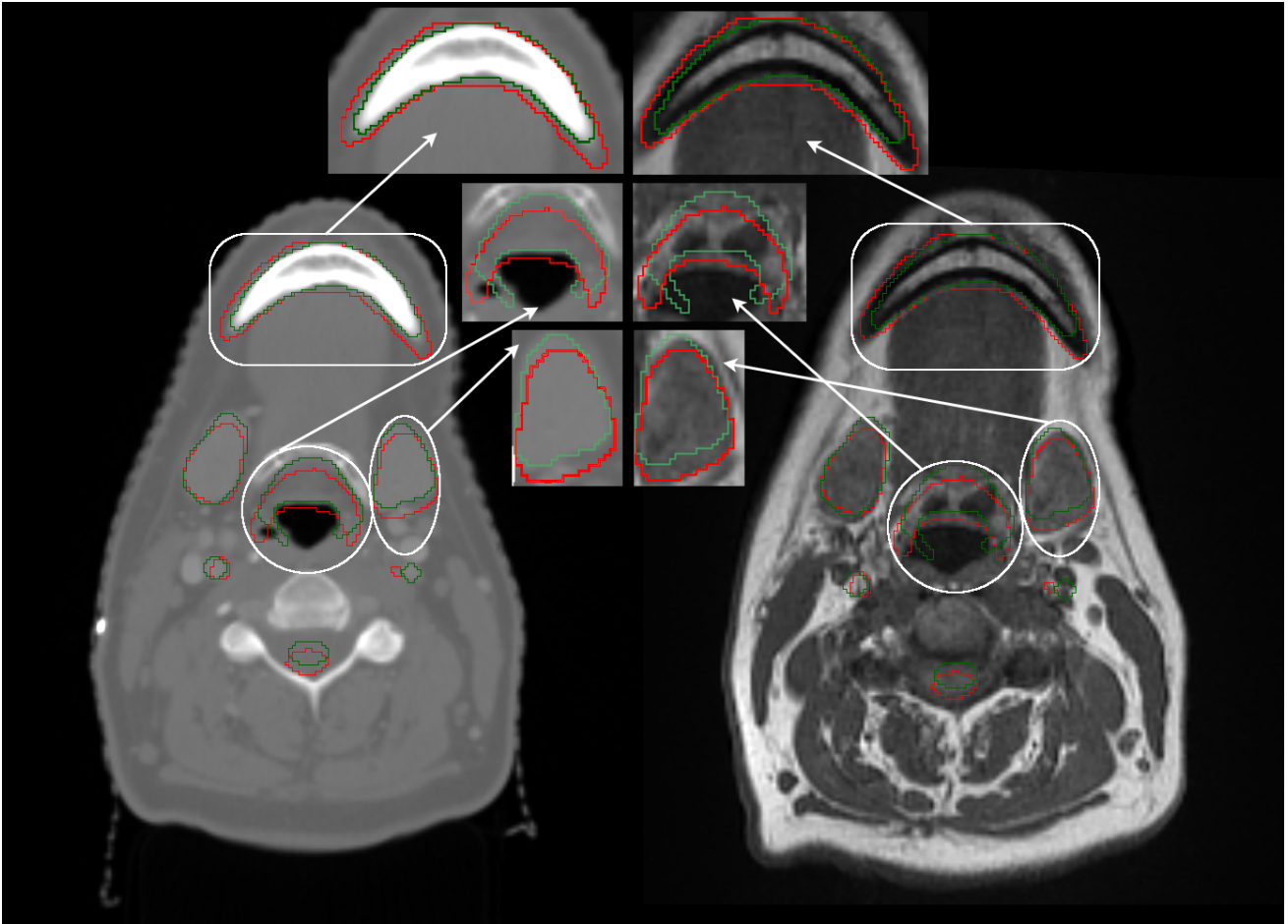


Figure 3: Prediction from MRI only, of a model trained with Modality Dropout. Left: Predicted (Red) and Ground Truth contours (Green) over the CT. Right: Prediction and Ground Truth contours overlaying the MRI. As seen on the CT, the ground truth matches the organs very well; however, the MRI-Only predictions are inaccurate. As observed on the MRI, the ground truth is not properly contouring its target organ, while the MRI-Only prediction is more accurate, particularly on the edges. This shows the incompatibility of the metrics to truly capture the model’s performance when utilizing only the MRI modality.

with Modality Dropout when CT information is missing. It can be observed that the prediction is faithful to the MRI scan but not to the CT scan and the ground truth, highlighting the noise introduced during the image registration process.

Table 3 presents the ablation study for combining the left and right OARs for bilateral OARs. It can be observed that the pipeline in which the model was trained on combined left and right OARs leads to better performance than the pipeline trained using separate left OARs and right OARs.

## 5 Discussion

The developed multimodal H&N OAR segmentation pipeline yielded the SOTA results in terms of Dice score and Hausdorff distance in the [Head and Neck Organ-At-Risk CT & MR Segmentation](#)

Performance	Left Right Organ Combination	
	Left Right OARs Combined	Not Combined
Dice Score $\uparrow$	<b>0.759 <math>\pm</math> 0.126</b>	0.749 $\pm$ 0.126
Hausdorff Distance 95 $\downarrow$	<b>3.233 <math>\pm</math> 1.664</b>	3.408 $\pm$ 1.78

Table 3: Segmentation metrics obtained by comparing predictions of our pipeline trained with left and right OARs combined or not. Results were first averaged over all cases and finally over all organs.  $\uparrow$  indicates that higher is best and  $\downarrow$  indicates smaller is best.

### Challenge.

The OAR with the lowest segmentation Dice Score is the Optic Chiasm, which is consistent with the fact that this small OAR is often difficult to see and manually segment, making it challenging for both manual and DL-based segmentations.

Our pipeline enhances nnU-Net preprocessing by integrating several advanced processing steps: rigid and non-rigid registration, tailored cropping strategies, and tissue-specific data processing. This enhanced pipeline employs a sequential combination of rigid and non-rigid registration to address the absence of annotations in certain modalities through the extrapolation of annotations from an alternative modality. Given the labor-intensive and costly nature of manual annotation across multiple data modalities, particularly for medical images, the proposed pipeline is anticipated to accelerate the DL-based approaches for multimodal segmentation tasks. Due to the extensive array of OARs and the stringent processing time constraints per patient, we opted for computationally efficient registration methods. We anticipate that integrating more precise, but computationally intensive, registration methods will improve model performance. Future research should explore the potential synergies among various registration techniques for the proposed pipeline for multimodal segmentation tasks.

The nnU-Net pipeline generates sub-patches from the input volumes. In our pipeline, the input volumes are cropped to algorithmically determined regions for OARs. It was empirically observed that incorporating this cropping approach accelerates the convergence and improves model performance. This acceleration results from the increased frequency of sub-patches containing OARs being fed to the model, leading to more frequent and relevant gradient updates.

The proposed pipeline also utilizes data processing that generates tissue-specific intensity values, specifically for bone and soft tissues in CT images. Generating these volumes provides a better contrast between tissue types. While the soft tissue volume is created to capture a detailed representation of soft tissue OARs, the volume dedicated to bone tissue aids in identifying OARs associated with bone tissues and also serves as a landmark for other soft tissue OARs.

The standard nnU-Net pipeline has been designed for unimodal image segmentation tasks and does not address scenarios with multimodal segmentation with missing data modalities. By incorporating Modality Dropout, the proposed pipeline extends the application of nnU-Net to multimodal image segmentation as well as allowing for missing data modalities, which is a common scenario in the medical imaging field.

In this study, the multimodality problem was approached using early fusion. Intermediate and late fusion in the latent space could mitigate the need for registration, which is time-consuming and computationally intensive. Late fusion in the latent space was studied by Podobnik et al. [19] for the same problem but showed no improvement compared to CT alone. In this study, the effectiveness of early fusion was observed both with and without Modality Dropout (see Table 2); however, further exploration of intermediate and late fusion for multimodal image segmentation

is suggested for future research.

The registration process of scans acquired at different times, whether rigid or non-rigid, is inherently imperfect due to the patient’s body and organ movements and changes. Since the ground truth contours are registered on the CT scan, this inherent imperfection forces the model to focus more on the CT modality, for which the ground truth contours are provided in this study. The experiments demonstrated that a visually high-quality registration, combined with a Modality Dropout during the training, can help a model use information from different modalities. In particular, the Modality Dropout augmentation had a considerable effect on the ability of the model to predict from the MRI modality, as shown in Table 2. Evaluating these findings in the context of other cancer sites—such as abdominal cancer, where organ movements are frequent—is suggested for future research.

Furthermore, as illustrated in Figure 3, even though a prediction can visually appear to be of high quality when overlaid over its corresponding MRI scan, when the model predicts using the MRI modality only, the imperfect registration of the MRI to the CT—which is consequently used as the ground truth contours—negatively affects the segmentation metrics. Therefore, these scores do not represent the ability of the model to precisely predict OAR segmentations from the MRI scans.

The stochastic nature of the optimization of the non-rigid, B-spline registration makes it computationally intensive accounting for a substantial part of the prediction time. DL-based registration could accelerate this step. Incorporating DL-based registration in the proposed pipeline is suggested for future research. The proposed pipeline can also predict only from a single modality. Therefore, if time is a constraint, users may choose to predict from only one modality to expedite the predictions; however, this might come at the cost of reduced precision.

Generating missing modalities from existing ones with DL [8, 9, 10, 11, 12, 13, 14, 15] could address the challenge of missing modalities and prevent the need for registration. However, this approach may come at the cost of a more complex and computationally intensive pipeline. Error made by such models could also negatively affect the final segmentations. Nevertheless, considering the pace of innovation in generative AI, incorporating these approaches is suggested for future research.

## 6 Conclusions

The proposed pipeline can effectively segment a wide range of OAR in H&N cancer patients from CT and MRI scans. It achieved the highest mean Dice score and mean Hausdorff Distance among all participants of the Head and Neck Organ- At-Risk CT & MR Segmentation Challenge, establishing a new SOTA. The pipeline can be used interchangeably with CT or MRI scans but works best with both modalities provided simultaneously. This pipeline can accelerate the OAR segmentation process, circumventing the tedious task of manual segmentation while eliminating inter-observer variability in applications like radiotherapy treatment planning.

## 7 Acknowledgments

This work was supported by the Canada Research Chair Program (grant #252135) and CHRP (NSERC+CIHR grant #170620). Computing resources were provided by the University of

British Columbia Cloud Innovation Centre, powered by Amazon Web Services (AWS). This research was also partly enabled by support provided by Calcul Quebec <https://www.calculquebec.ca/en/>, the Digital Research Alliance of Canada <https://alliancecan.ca/>, and the University of Calgary Advanced Research Computing (ARC) Cluster [https://rcs.ucalgary.ca/RCS\\_Home\\_Page](https://rcs.ucalgary.ca/RCS_Home_Page). Additionally, this research was made possible by generous support from Google's exploreCSR program.

## References

- [1] A. Argiris et al. “Head and neck cancer”. eng. In: *Lancet (London, England)* 371.9625 (May 2008), pp. 1695–1709. ISSN: 1474-547X. DOI: [10.1016/S0140-6736\(08\)60728-X](https://doi.org/10.1016/S0140-6736(08)60728-X).
- [2] V. Grégoire, J. A. Langendijk, and S. Nuyts. “Advances in Radiotherapy for Head and Neck Cancer”. en. In: *Journal of Clinical Oncology* 33.29 (Oct. 2015), pp. 3277–3284. ISSN: 0732-183X, 1527-7755. DOI: [10.1200/JCO.2015.61.2994](https://doi.org/10.1200/JCO.2015.61.2994).
- [3] J. J. Caudell et al. “The future of personalised radiotherapy for head and neck cancer”. eng. In: *The Lancet. Oncology* 18.5 (May 2017), e266–e273. ISSN: 1474-5488. DOI: [10.1016/S1470-2045\(17\)30252-8](https://doi.org/10.1016/S1470-2045(17)30252-8).
- [4] J. Wong et al. “Comparing deep learning-based auto-segmentation of organs at risk and clinical target volumes to expert inter-observer variability in radiotherapy planning”. eng. In: *Radiotherapy and Oncology: Journal of the European Society for Therapeutic Radiology and Oncology* 144 (Mar. 2020), pp. 152–158. ISSN: 1879-0887. DOI: [10.1016/j.radonc.2019.10.019](https://doi.org/10.1016/j.radonc.2019.10.019).
- [5] G. Podobnik et al. “HaN-Seg: The head and neck organ-at-risk CT and MR segmentation dataset”. eng. In: *Medical Physics* 50.3 (Mar. 2023), pp. 1917–1927. ISSN: 2473-4209. DOI: [10.1002/mp.16197](https://doi.org/10.1002/mp.16197).
- [6] V. S. Khoo et al. “Comparison of MRI with CT for the radiotherapy planning of prostate cancer: a feasibility study.” en. In: *The British Journal of Radiology* 72.858 (June 1999), pp. 590–597. ISSN: 1748-880X, 0007-1285. DOI: [10.1259/bjr.72.858.10560342](https://doi.org/10.1259/bjr.72.858.10560342).
- [7] R. F. Verhaart et al. “The relevance of MRI for patient modeling in head and neck hyperthermia treatment planning: A comparison of CT and CT-MRI based tissue segmentation on simulated temperature”. en. In: *Medical Physics* 41.12 (Dec. 2014), p. 123302. ISSN: 0094-2405, 2473-4209. DOI: [10.1118/1.4901270](https://doi.org/10.1118/1.4901270).
- [8] Y. Huo et al. “SynSeg-Net: Synthetic Segmentation Without Target Modality Ground Truth”. In: *IEEE Transactions on Medical Imaging* 38.4 (2019), pp. 1016–1025. DOI: [10.1109/TMI.2018.2876633](https://doi.org/10.1109/TMI.2018.2876633).
- [9] K. Li et al. “Towards Cross-Modality Medical Image Segmentation with Online Mutual Knowledge Distillation”. In: *Proceedings of the AAAI Conference on Artificial Intelligence* 34.01 (Apr. 2020), pp. 775–783. DOI: [10.1609/aaai.v34i01.5421](https://doi.org/10.1609/aaai.v34i01.5421).
- [10] Y. Liu et al. “Head and neck multi-organ auto-segmentation on CT images aided by synthetic MRI”. In: *Medical physics* 47.9 (2020), pp. 4294–4302.
- [11] J. Jiang et al. “Self-derived organ attention for unpaired CT-MRI deep domain adaptation based MRI segmentation”. In: *Physics in Medicine & Biology* 65.20 (2020), p. 205001.
- [12] Y. Lei et al. “CT prostate segmentation based on synthetic MRI-aided deep attention fully convolution network”. In: *Medical physics* 47.2 (2020), pp. 530–540.
- [13] J. Jiang et al. “Tumor-aware, adversarial domain adaptation from CT to MRI for lung cancer segmentation”. In: *Medical Image Computing and Computer Assisted Intervention—MICCAI 2018: 21st International Conference, Granada, Spain, September 16-20, 2018, Proceedings, Part II 11*. Springer. 2018, pp. 777–785.

- [14] J. Jue et al. “Integrating cross-modality hallucinated MRI with CT to aid mediastinal lung tumor segmentation”. In: *Medical image computing and computer assisted intervention–MICCAI 2019: 22nd International Conference, Shenzhen, China, October 13–17, 2019, Proceedings, Part VI 22*. Springer. 2019, pp. 221–229.
- [15] X. Yang et al. “Synthetic MRI-aided multi-organ CT segmentation for head and neck radiotherapy treatment planning”. In: *International Journal of Radiation Oncology, Biology, Physics* 108.3 (2020), e341.
- [16] Q. Dou et al. “PnP-AdaNet: Plug-and-Play Adversarial Domain Adaptation Network at Unpaired Cross-Modality Cardiac Segmentation”. In: *IEEE Access* 7 (2019), pp. 99065–99076. DOI: [10.1109/ACCESS.2019.2929258](https://doi.org/10.1109/ACCESS.2019.2929258).
- [17] V. V. Valindria et al. “Multi-modal Learning from Unpaired Images: Application to Multi-organ Segmentation in CT and MRI”. In: *2018 IEEE Winter Conference on Applications of Computer Vision (WACV)*. 2018, pp. 547–556. DOI: [10.1109/WACV.2018.00066](https://doi.org/10.1109/WACV.2018.00066).
- [18] W. Yang et al. “An Effective MR-Guided CT Network Training for Segmenting Prostate in CT Images”. In: *IEEE Journal of Biomedical and Health Informatics* 24.8 (2020), pp. 2278–2291. DOI: [10.1109/JBHI.2019.2960153](https://doi.org/10.1109/JBHI.2019.2960153).
- [19] G. Podobnik et al. “Multimodal CT and MR segmentation of head and neck organs-at-risk”. In: *International Conference on Medical Image Computing and Computer-Assisted Intervention*. Springer. 2023, pp. 745–755.
- [20] F. Isensee et al. “nnU-Net: a self-configuring method for deep learning-based biomedical image segmentation”. en. In: *Nature Methods* 18.2 (Feb. 2021), pp. 203–211. ISSN: 1548-7105. DOI: [10.1038/s41592-020-01008-z](https://doi.org/10.1038/s41592-020-01008-z).
- [21] B. C. Lowekamp et al. “The Design of SimpleITK”. eng. In: *Frontiers in Neuroinformatics* 7 (2013), p. 45. ISSN: 1662-5196. DOI: [10.3389/fninf.2013.00045](https://doi.org/10.3389/fninf.2013.00045).
- [22] D. Mattes et al. “Nonrigid multimodality image registration”. In: 4322 (July 2001). ADS Bibcode: 2001SPIE.4322.1609M, pp. 1609–1620. DOI: [10.1117/12.431046](https://doi.org/10.1117/12.431046).
- [23] D. Mattes et al. “PET-CT image registration in the chest using free-form deformations”. eng. In: *IEEE transactions on medical imaging* 22.1 (Jan. 2003), pp. 120–128. ISSN: 0278-0062. DOI: [10.1109/TMI.2003.809072](https://doi.org/10.1109/TMI.2003.809072).
- [24] N. Neverova et al. “ModDrop: Adaptive Multi-Modal Gesture Recognition”. In: *IEEE Transactions on Pattern Analysis and Machine Intelligence* 38.8 (2016), pp. 1692–1706. DOI: [10.1109/TPAMI.2015.2461544](https://doi.org/10.1109/TPAMI.2015.2461544).
- [25] X. Li et al. “Multi-scale and Modality Dropout Learning for Intervertebral Disc Localization and Segmentation”. In: *Computational Methods and Clinical Applications for Spine Imaging*. Ed. by J. Yao et al. Cham: Springer International Publishing, 2016, pp. 85–91. ISBN: 978-3-319-55050-3.
- [26] H. Liu et al. “ModDrop++: A Dynamic Filter Network with Intra-subject Co-training for Multiple Sclerosis Lesion Segmentation with Missing Modalities”. In: *Medical Image Computing and Computer Assisted Intervention – MICCAI 2022*. Ed. by L. Wang et al. Cham: Springer Nature Switzerland, 2022, pp. 444–453. ISBN: 978-3-031-16443-9.

- [27] R. H. Byrd et al. “A Limited Memory Algorithm for Bound Constrained Optimization”. In: *SIAM Journal on Scientific Computing* 16.5 (1995), pp. 1190–1208. DOI: [10.1137/0916069](https://doi.org/10.1137/0916069). eprint: <https://doi.org/10.1137/0916069>.
- [28] C. Zhu et al. “Algorithm 778: L-BFGS-B: Fortran subroutines for large-scale bound-constrained optimization”. In: *ACM Transactions on mathematical software (TOMS)* 23.4 (1997), pp. 550–560.

## A Registration pipeline

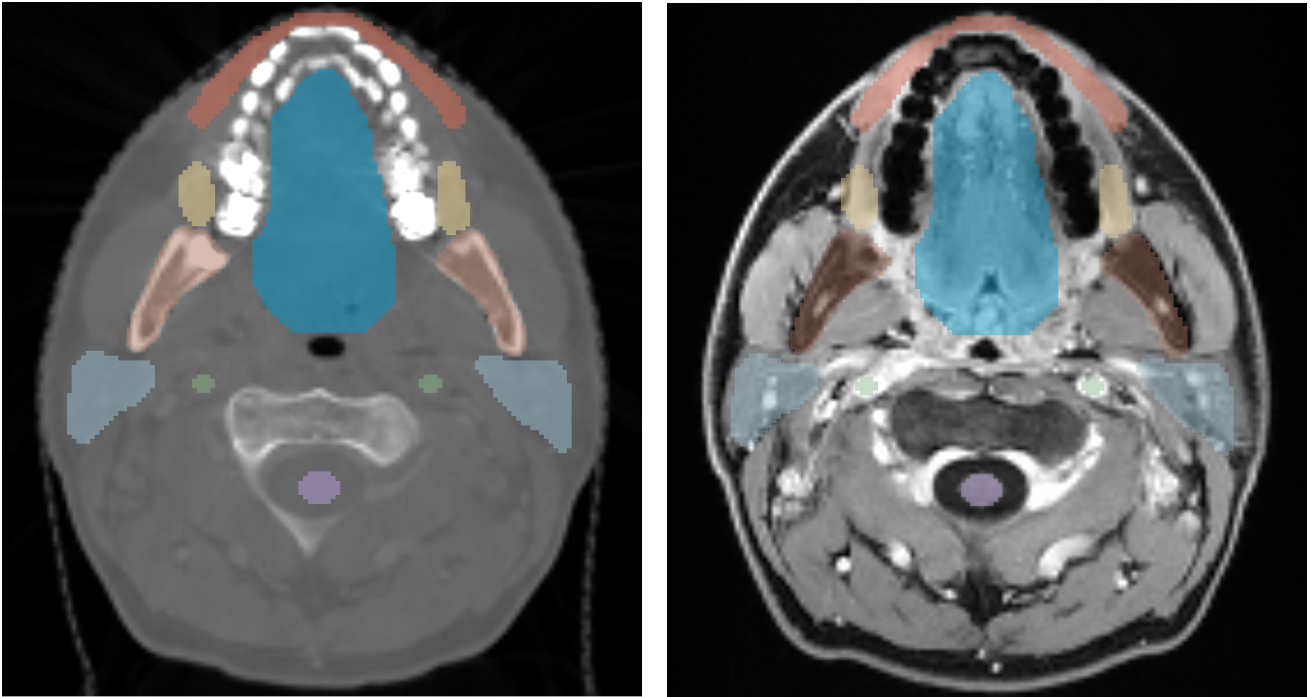
For both the rigid and non-rigid registration, the linear interpolator was used to transform the MRI volume during optimization, and a cubic B-spline interpolator was used for final registration. Furthermore, both registrations used a multi-resolution framework and the same parameters to compute the MI: 50 histogram bins were used, and 1% of volume points were randomly sampled.

Two different initial translations, applied prior to rigid registration, were considered: aligning the centers of mass of the two volumes, computed from the moments of gray level values, and aligning the geometrical centers of the two volumes. The gradient descent line search algorithm was used to minimize the negative MI between the MRI and CT volumes by optimizing the transformation parameters of the MRI volume. A learning rate of 5.0 was used for the line search gradient descent with an upper limit of 5.0. An early stopping approach was used to terminate the optimization process if the improvement in mutual information over the past ten steps was less than 0.0001. In the rare case where randomly sampled points would lead to an unsatisfactory registration (quality threshold for MI was set to -0.35), registration was performed once more. MI was computed again after each of the two rigid registration, but this time considering every voxel of the volume and 100 histogram bins. This measure is referred to as the complete MI. The initialization yielding the best complete MI for the rigid registration was used.

After these steps, a non-rigid registration was performed. A mesh of  $5 \times 5 \times 5$  cubes overlaid on the MRI volume was deformed with cubic B-splines. A Limited memory Broyden-Fletcher-Goldfarb-Shannon (L-BFGS) algorithm with simple bounds [27, 28] was used to optimize the B-splines parameters, with upper and lower bounds of 5.0 and -5.0, respectively, for 20 optimizer iterations at each resolution. If non-rigid registration resulted in a better complete MI, its parameters were used to resample the MRI volume; otherwise, the parameters of the best rigid registration were used.



## B Registration Results



(a) Annotated CT scan.

(b) Annotated registered MRI scan.

Figure 4: CT and registered MRI of one patient of our training dataset, with ground truth contour overlaid. Blue corresponds to the oral cavity, brown is the mandible, yellow is the buccal mucosa, light blue is the parotid gland, purple is the spinal cord, red corresponds to the lips and green to the carotid arteries. The contours overlaid on both modalities are an indicator of the quality of the registration. To the non-specialist’s eye, all contours appear correctly aligned to the MRI volume.

As no ground truth alignment was provided, reliably evaluating the registration quality without using manually placed anatomical markers was impossible. However, upon visual inspection, the registration performed well on all patients in our dataset. Figure 4 showcases the registration for one patient.

## C Detailed Challenge Submission Results

Organ at risk	Dice Score $\uparrow$	Hausdorff Distance $\downarrow$	Organ at risk	Dice Score $\uparrow$	Hausdorff Distance $\downarrow$
Lips	$0.754 \pm 0.083$	$6.188 \pm 3.22$	Cervical esophagus	$0.609 \pm 0.114$	<b><math>7.661 \pm 3.727</math></b>
Anterior eyeball segment - Left	$0.788 \pm 0.067$	$2.206 \pm 0.646$	<b>Optic chiasm</b>	<b><math>0.411 \pm 0.182</math></b>	$4.289 \pm 1.912$
Anterior eyeball segment - Right	$0.803 \pm 0.055$	$2.041 \pm 0.741$	Buccal mucosa	$0.71 \pm 0.084$	$5.501 \pm 2.74$
Posterior eyeball segment - Left	$0.93 \pm 0.016$	$1.569 \pm 0.407$	Thyroid gland	$0.891 \pm 0.046$	$2.616 \pm 2.268$
Posterior eyeball segment - Right	$0.924 \pm 0.015$	$1.739 \pm 0.486$	<b>Mandible bone</b>	<b><math>0.952 \pm 0.017</math></b>	<b><math>1.289 \pm 1.037</math></b>
Larynx—supraglottic	$0.758 \pm 0.087$	$3.01 \pm 1.426$	Submandibular gland - Left	$0.85 \pm 0.092$	$3.42 \pm 2.338$
Arytenoids	$0.621 \pm 0.137$	$3.358 \pm 2.606$	Submandibular gland - Right	$0.845 \pm 0.069$	$4.071 \pm 3.094$
Cochlea - Left	$0.766 \pm 0.085$	$1.502 \pm 0.83$	Lacrimal gland - Left	$0.665 \pm 0.107$	$2.825 \pm 1.048$
Cochlea - Right	$0.755 \pm 0.097$	$1.777 \pm 0.872$	Lacrimal gland - Right	$0.639 \pm 0.137$	$3.742 \pm 1.73$
Larynx supraglottic	$0.813 \pm 0.068$	$3.579 \pm 1.398$	Oral cavity	$0.899 \pm 0.042$	$5.13 \pm 2.367$
Parotid gland - Left	$0.865 \pm 0.029$	$4.846 \pm 1.758$	Pituitary gland	$0.719 \pm 0.107$	$2.298 \pm 0.919$
Parotid gland - Right	$0.847 \pm 0.041$	$5.515 \pm 2.362$	Cricopharyngeal inlet	$0.642 \pm 0.116$	$6.426 \pm 3.459$
Optic Nerve - Left	$0.709 \pm 0.081$	$2.218 \pm 0.768$	Brainstem	$0.85 \pm 0.03$	$5.026 \pm 1.189$
Optic nerve - Right	$0.741 \pm 0.05$	$2.656 \pm 1.597$	Carotid artery - Left	$0.849 \pm 0.042$	$3.295 \pm 4.407$
Spinal cord	$0.825 \pm 0.039$	$2.126 \pm 1.791$	Carotid artery - Right	$0.87 \pm 0.029$	$1.743 \pm 1.951$

Table 4: Mean Dice score obtained on the test patients of the [Head and Neck Organ-At-Risk CT & MR Segmentation Challenge](#). These scores were obtained by submitting to the challenge platform and are available on [the challenge website](#). The reported measures are in the form of mean  $\pm$  standard deviation.  $\uparrow$  indicates that higher is best and  $\downarrow$  indicates smaller is best.